

WMOE-CLIP: WAVELET-ENHANCED MIXTURE-OF-EXPERTS PROMPT LEARNING FOR ZERO-SHOT ANOMALY DETECTION

Peng Chen, Chao Huang*

School of Cyber Science and Technology, Shenzhen Campus of Sun Yat-sen University, Shenzhen
23pchen@stu.edu.cn, huangch253@mail.sysu.edu.cn

ABSTRACT

Vision–language models have recently shown strong generalization in zero-shot anomaly detection (ZSAD), enabling the detection of unseen anomalies without task-specific supervision. However, existing approaches typically rely on fixed textual prompts, which struggle to capture complex semantics, and focus solely on spatial-domain features, limiting their ability to detect subtle anomalies. To address these challenges, we propose a wavelet-enhanced mixture-of-experts prompt learning method for ZSAD. Specifically, a variational autoencoder is employed to model global semantic representations and integrate them into prompts to enhance adaptability to diverse anomaly patterns. Wavelet decomposition extracts multi-frequency image features that dynamically refine textual embeddings through cross-modal interactions. Furthermore, a semantic-aware mixture-of-experts module is introduced to aggregate contextual information. Extensive experiments on 14 industrial and medical datasets demonstrate the effectiveness of the proposed method.

Index Terms— anomaly detection, prompt learning, vision-language models, zero-shot learning

1. INTRODUCTION

Anomaly detection aims to identify instances that deviate from normal patterns and has been widely applied across various domains, including industrial [1, 2] and medical scenarios [3, 4]. Due to the diversity of anomaly types and the scarcity of abnormal samples, traditional approaches typically adopt unsupervised strategies. However, in practical applications, acquiring sufficient training data remains a major challenge [5]. For example, patient data may be restricted by privacy regulations [6], and new production lines may lack representative samples. ZSAD addresses this by detecting unseen anomalies using auxiliary datasets. However, achieving robust generalization across diverse product categories and complex environments remains a persistent challenge.

This work was supported in part by the National Natural Science Foundation of China (No.62301621), Shenzhen Science and Technology Program (No. 20231121172359002, 2023A008), Shenzhen General Research Project (No. JCYJ20241202125904007), and Guangdong Basic and Applied Basic Research Foundation (No. 2025A1515011398).

Vision-language models like CLIP have advanced ZSAD by leveraging large-scale image–text pretraining [2], enabling robust generalization to unseen categories [7]. For example, WinCLIP [1] identifies potential anomalous regions by measuring the similarity between multi-scale visual features and manually crafted textual prompts. To reduce reliance on handcrafted prompts, AnomalyCLIP [6] introduces learnable class-agnostic textual prompts with a V-V attention, enhancing zero-shot performance. Furthermore, AdaCLIP [4] employs a hybrid prompting strategy that combines dynamic and static prompts to improve generalization, while AA-CLIP [2] leverages a two-stage training paradigm to better adapt CLIP for anomaly detection. However, two critical issues remain. First, fixed prompts provide sparse semantic information, potentially leading to overfitting within a constrained semantic space. Second, exclusive reliance on spatial information limits the model’s ability to detect subtle defects.

To address these challenges, we propose WMOE-CLIP, a novel wavelet-enhanced mixture-of-experts prompt learning approach based on CLIP for ZSAD. Our method improves anomaly detection by reinforcing the alignment and adaptability of image–text representations. Specifically, a variational autoencoder (VAE) is employed to sample from the global feature distribution, embedding rich semantic information into the prompts. To further strengthen multimodal alignment, wavelet decomposition extracts multi-frequency image features, which dynamically refine textual embeddings via cross-attention, enabling the detection of subtle anomalies. Additionally, a semantic-aware mixture-of-experts module aggregates contextual information, further enhancing the model’s capability to recognize diverse anomaly patterns.

In summary, our contributions are as follows: 1) We propose WMOE-CLIP, a novel CLIP-based method that enhances image–text interactions, effectively improving both the accuracy and generalization of zero-shot anomaly detection. 2) We leverage a VAE to model global feature distributions and incorporate frequency-domain features to strengthen cross-modal interactions. Additionally, we introduce a semantic-aware mixture-of-experts module to aggregate contextual semantic information. 3) Extensive experiments on 14 industrial and medical datasets demonstrate that WMOE-CLIP achieves state-of-the-art performance.

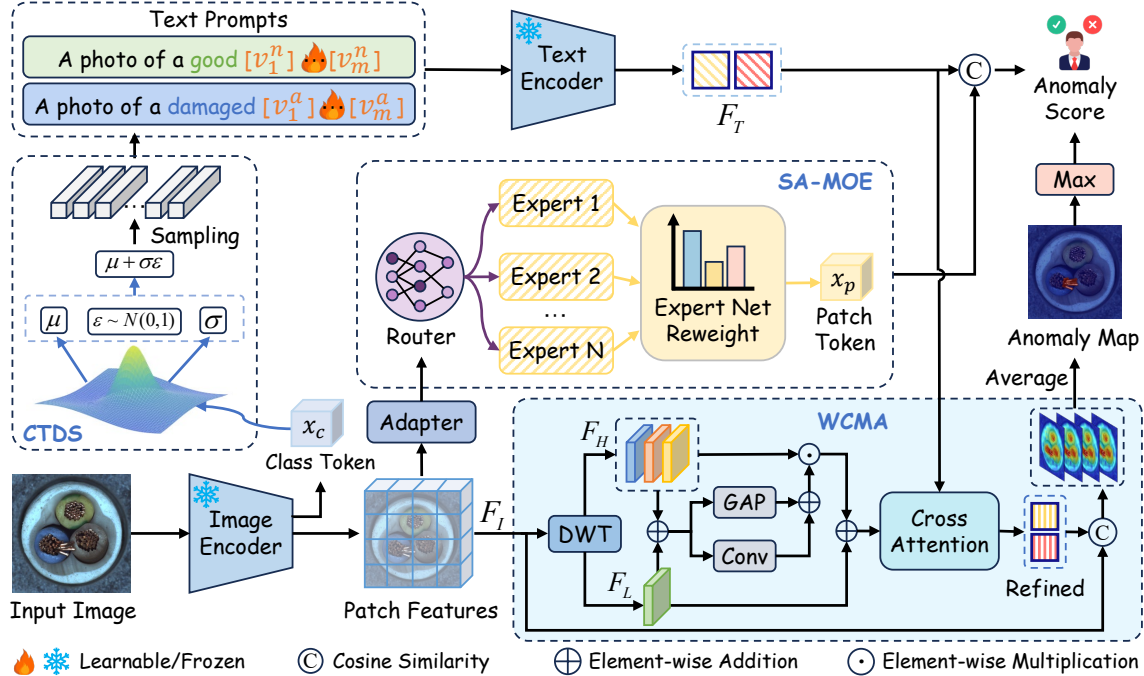


Fig. 1. Framework of WMoE-CLIP. CTDS leverages a VAE to model global semantic features, enhancing the adaptability of text embeddings. WCMA dynamically updates text embeddings using wavelet-based frequency features. SA-MoE employs a mixture-of-experts model to capture rich contextual information, further enhancing robust image-level anomaly scoring.

2. METHODOLOGY

In this paper, we propose WMoE-CLIP, a wavelet-enhanced mixture-of-experts model built upon CLIP for ZSAD. As illustrated in Fig. 1, WMoE-CLIP comprises three core components: Class Token Distribution Sampling (CTDS), Wavelet-Enhanced Cross-Modal Attention (WCMA), and Semantic-Aware Mixture-of-Experts (SA-MoE). Given an input image $I \in \mathbb{R}^{h \times w \times 3}$, a frozen image encoder extracts the global class token $x_c \in \mathbb{R}^C$ and patch features $F_I \in \mathbb{R}^{H \times W \times C}$, where C denotes the embedding dimension. CTDS models the latent distribution of the global features and integrates them into the prompts. To facilitate cross-modal alignment, WCMA dynamically refines text embeddings guided by frequency-domain image features. Furthermore, SA-MoE adaptively selects experts to aggregate contextual semantic information.

2.1. Class Token Distribution Sampling

Existing approaches typically rely on coarse-grained prompts, which lack adaptability to image-specific visual contexts. To address this limitation, we propose CTDS, which leverages a VAE to model the global distribution and integrate the sampled representations into learnable prompt embeddings. As shown in Fig. 1, the global class token x_c from the image encoder is projected into a latent space via two fully connected layers to obtain the mean and variance, from which a latent

variable is sampled via reparameterization, formulated as:

$$\begin{aligned} \mu_c &= W_\mu \text{MLP}(x_c), & \log \sigma_c^2 &= W_\sigma \text{MLP}(x_c), \\ s_c &= \mu_c + \epsilon \odot \sigma_c, & \epsilon &\sim \mathcal{N}(0, I), \end{aligned} \quad (1)$$

where W_μ, W_σ are learnable parameters, and \odot represents element-wise multiplication. The latent representation s_c is passed through a decoder (an MLP) to obtain the reconstructed global feature $r \in \mathbb{R}^C$, and the latent distribution is regularized using the Kullback-Leibler divergence:

$$\mathcal{L}_{\text{KL}} = -\frac{1}{2} \sum_{i=1}^C \left(1 + \log(\sigma_c^i)^2 - (\mu_c^i)^2 - (\sigma_c^i)^2 \right). \quad (2)$$

In addition, to encourage consistency between the original and reconstructed features, we employ a reconstruction loss:

$$\mathcal{L}_{\text{rec}} = \|r - x_c\|^2. \quad (3)$$

We introduce the template “a photo of a good/damaged $[v_i^n]/[v_i^a]$ ”, where $[v_i^n]$ and $[v_i^a]$ are learnable vectors encoding category-specific semantics. $\{r_i\}_{i=1}^m$ are sampled from the latent space and are fused with the corresponding vector as $g(r_i, v_i) = r_i + v_i$, which replaces v_i in the prompt. The normal and abnormal prompts, P^n and P^a , are defined as:

$$\begin{aligned} P^n &= \text{a photo of a good } g(r_1, v_1^n), \dots, g(r_m, v_m^n), \\ P^a &= \text{a photo of a damaged } g(r_1, v_1^a), \dots, g(r_m, v_m^a). \end{aligned} \quad (4)$$

The constructed prompts are fed into the text encoder to obtain the corresponding text embeddings $F_T \in \mathbb{R}^{2 \times C}$.

2.2. Wavelet-Enhanced Cross-Modal Attention

Incorporating image-specific features into text embeddings complicates alignment with image features. Additionally, high-frequency components preserve rich details crucial for detecting subtle anomalies. Therefore, we propose WCMA to enhance the adaptability of text embeddings to image features. Specifically, a Haar wavelet transform is applied to decompose F_I into low-frequency information (F_L) and high-frequency components along the horizontal (F_{LH}), vertical (F_{HL}), and diagonal (F_{HH}) directions. The high-frequency sub-bands are then aggregated ($F_H = F_{LH} + F_{HL} + F_{HH}$) to form an overall high-frequency component.

To capture high-frequency information, we jointly model global and local dependencies across multi-frequency components. $F_L \in \mathbb{R}^{H \times W \times C}$ and $F_H \in \mathbb{R}^{H \times W \times C}$ are combined, with global channel representations obtained via global average pooling (GAP) and local representations via pointwise convolution. These are then fused to generate the attention weights W_h for the high-frequency component:

$$W_h = \sigma(W_1 \cdot \text{ReLU}(\text{GAP}(F_L + F_H)) + W_2 \cdot \text{ReLU}(\delta_p(F_L + F_H))), \quad (5)$$

where $\sigma(\cdot)$ denotes the sigmoid function, W_1 and W_2 are linear layers, and δ_p indicates the pointwise convolution. The frequency-enhanced image representation $F_p \in \mathbb{R}^{H \times W \times C}$ is obtained by reweighting high-frequency features and aggregating them with the low-frequency features:

$$F_p = F_H \odot W_h + F_L, \quad (6)$$

where \odot denotes element-wise multiplication. To adapt text embeddings to patch features, we employ a cross-attention, where text queries interact with the image keys and values:

$$F'_T = \text{softmax}\left(Q_T K_I^\top / \sqrt{C}\right) V_I, \quad (7)$$

where $F'_T \in \mathbb{R}^{2 \times C}$ are the refined text embeddings. $Q_T = F_T W_q$, $K_I = F_p W_k$, $V_I = F_p W_v$, and W_q, W_k, W_v are learnable parameters. The anomaly map $M \in \mathbb{R}^{h \times w}$ is computed from the similarity between F'_T and the patch features.

2.3. Semantic-Aware Mixture-of-Experts

To enable more reliable anomaly score computation, we propose SA-MoE, which adaptively aggregates global semantic information from contextual features. Given patch features from multiple layers, we introduce an Adapter consisting of a linear layer followed by global average pooling. The linear layer projects patch features into a unified space. The features are then concatenated along the channel dimension, and global average pooling across the spatial dimensions yields the contextual representation $x_a \in \mathbb{R}^C$.

SA-MoE consists of a routing gate $\mathcal{G}(\cdot)$ and N expert networks $E_n(\cdot)$, which dynamically activate the Top- k experts

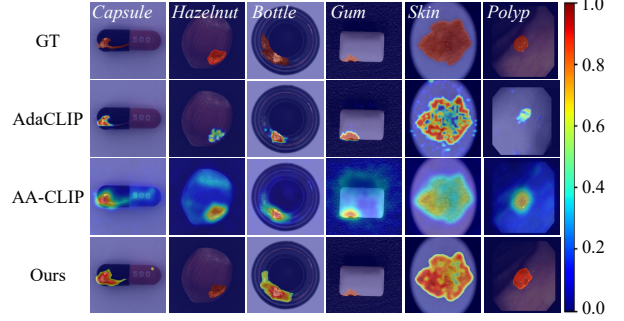


Fig. 2. Comparative visualization of anomaly localization.

to aggregate global semantics. Specifically, the routing gate computes a relevance score $s_n = \mathcal{G}(x_a)$ for each expert based on x_a . The enhanced patch features are obtained by aggregating the outputs of the selected experts as follows:

$$x_p = \sum_k w_k E_k(x_a) \quad (8)$$

where w_k denotes the normalized routing weight of the k -th expert. To further consolidate semantic information, x_p is integrated with the class token: $x_{cls} = x_p + x_c$. The anomaly score s_{txt} is then computed as the similarity between x_{cls} and the text feature F_T . The final image-level anomaly score is obtained by combining s_{txt} with the maximum value of the anomaly map: $\hat{s} = s_{txt} + \max(M)$.

2.4. Loss Function

We jointly employ global and local losses to guide optimization. The global loss adopts the binary cross-entropy to supervise image-level predictions, while the local loss combines Focal and Dice losses to optimize pixel-level predictions:

$$\mathcal{L}_{global} = \text{BCE}(S_{gt}, \hat{s}), \quad (9)$$

$$\mathcal{L}_{local} = \sum_l \text{Focal}(M_l, M_{gt}) + \sum_l \text{Dice}(M_l, M_{gt}), \quad (10)$$

where $S_{gt} \in \{0, 1\}$ and $M_{gt} \in \mathbb{R}^{h \times w}$ denote the ground-truth label and pixel-level mask. The overall objective function is:

$$\mathcal{L} = \mathcal{L}_{global} + \mathcal{L}_{local} + \mathcal{L}_{KL} + \mathcal{L}_{rec}. \quad (11)$$

3. EXPERIMENTS

3.1. Experimental Setup

Datasets. We conducted experiments on 14 publicly available datasets, including six industrial datasets: MVTEC-AD [8], VisA [9], BTAD [10], KSDD2 [11], DAGM [12], and DTD-Synthetic [13]; and eight medical datasets: HeadCT [14], BrainMRI [15], BR35H [6], ISIC [16], CVC-ColonDB [17], CVC-ClinicDB [18], Endo [19], and Kvasir [3].

Table 1. Comparison of ZSAD performance. The best results are highlighted in red, and the second-best are marked in blue.

Domain	Metric	Dataset	WinCLIP	CLIP-AD	AnomalyCLIP	Ada-CLIP	AA-CLIP	WMoE-CLIP
			CVPR2023	IJCAI2024	ICLR2024	ECCV2024	CVPR2025	—
Industrial	Image-level (AUROC,F1-Max, AP)	MVTec-AD	(91.8, 92.9 , 95.1)	(89.8, 91.1, 95.3)	(91.5, 92.8, 96.2)	(92.0 , 92.7, 96.4)	(90.5, 91.4, 95.6)	(92.4 , 93.2 , 96.9)
		VisA	(78.1, 79.0, 77.5)	(79.8, 79.2, 84.3)	(82.1, 80.4, 85.4)	(83.0, 81.6 , 84.9)	(84.6 , 78.7, 83.4)	(87.3 , 84.4 , 90.0)
		BTAD	(83.3, 81.0, 84.1)	(85.8, 81.7, 85.2)	(89.1, 86.0, 91.1)	(91.6, 88.9, 92.4)	(93.8 , 92.8 , 97.1)	(92.6 , 95.0 , 97.8)
		KSDD2	(93.5, 71.4, 77.9)	(95.2, 84.4, 88.2)	(92.1, 71.0, 77.8)	(95.9 , 84.5, 95.9)	(95.8, 91.4 , 96.8)	(96.8 , 91.5 , 97.4)
		DAGM	(89.6, 86.4, 90.4)	(90.8, 88.4, 90.5)	(95.6, 93.2, 94.6)	(96.5 , 94.1 , 95.7)	(94.3, 81.7, 84.2)	(96.7 , 93.4 , 95.9)
	DTD-Synthetic	(93.2, 94.3, 92.6)	(91.5, 91.8, 96.8)	(93.5 , 94.5 , 97.0)	(92.8, 92.2, 97.0)	(91.4, 93.3, 97.2)	(95.0 , 95.6 , 98.4)	
	Pixel-level (AUROC,PRO, AP)	MVTec-AD	(85.1, 64.6, 18.0)	(89.8, 70.6, 40.0)	(91.1, 81.4 , 34.5)	(86.8, 33.8, 38.1)	(91.9 , 61.9, 45.4)	(92.1 , 86.8 , 48.1)
		VisA	(79.6, 56.8, 5.0)	(95.0, 86.9, 26.3)	(95.5 , 87.0 , 21.3)	(95.1, 71.3, 29.2)	(95.5 , 46.3, 25.0)	(95.6 , 90.1 , 28.9)
		BTAD	(71.4, 32.8, 11.2)	(93.1, 59.8, 46.7)	(93.3 , 69.3 , 42.0)	(87.7, 17.1, 36.6)	(96.1 , 34.4, 46.3)	(93.3 , 75.1 , 46.9)
		KSDD2	(97.9, 91.2, 17.1)	(99.3, 85.4, 58.9)	(99.4, 92.7 , 41.8)	(96.1, 70.8, 56.4)	(99.5 , 68.8, 43.7)	(99.6 , 98.4 , 72.5)
DAGM		(83.2, 55.4, 3.1)	(99.0, 83.1, 40.7)	(99.1 , 93.6 , 29.5)	(97.0, 40.9, 44.2)	(96.3, 31.4, 45.9)	(99.5 , 98.2 , 47.6)	
DTD-Synthetic	(83.9, 57.8, 11.6)	(97.1, 68.7, 62.3)	(97.9 , 92.3 , 52.4)	(94.1, 24.9, 52.8)	(96.4, 62.8, 62.8)	(98.2 , 94.7 , 71.6)		
Medical	Image-level (AUROC,F1-Max, AP)	HeadCT	(83.7, 78.8, 81.6)	(93.8, 90.5, 92.2)	(95.3, 89.7, 95.2)	(93.3, 86.5, 92.2)	(96.8 , 93.4 , 95.3)	(98.2 , 92.9 , 98.1)
		BrainMRI	(92.0, 84.2, 90.7)	(92.8, 88.7, 85.5)	(96.1 , 92.3, 92.3)	(94.9, 90.4, 94.2)	(94.1, 93.5 , 93.3)	(96.4 , 95.5 , 97.6)
		Br35H	(80.5, 74.1, 82.2)	(96.0, 90.8, 95.5)	(97.3 , 92.4 , 96.1)	(95.7, 89.1, 95.7)	(96.2, 91.5, 94.2)	(98.1 , 95.3 , 98.2)
	Pixel-level (AUROC,PRO, AP)	ISIC	(83.3, 55.1, 62.4)	(81.6, 29.0, 65.5)	(88.4, 78.1, 74.4)	(85.4, 5.3, 70.6)	(93.8 , 88.5 , 85.9)	(94.2 , 89.2 , 87.0)
		ColonDB	(64.8, 28.4, 14.3)	(80.3, 58.8, 23.7)	(81.9, 71.4, 31.3)	(79.3, 6.5, 26.2)	(83.6 , 76.9 , 32.1)	(84.3 , 77.7 , 36.3)
		ClinicDB	(70.7, 32.5, 19.4)	(85.8, 69.7, 39.0)	(85.9, 69.6, 42.2)	(84.3, 14.6, 36.0)	(89.5 , 79.7 , 56.5)	(90.1 , 80.6 , 58.3)
		Endo	(68.2, 28.3, 23.8)	(85.6, 57.0, 51.7)	(86.3, 67.3, 50.4)	(84.0, 10.5, 44.8)	(90.2 , 77.0 , 60.7)	(91.0 , 78.9 , 65.0)
		Kvasir	(69.8, 31.0, 27.5)	(82.5, 48.1, 46.2)	(81.8, 53.8, 42.5)	(79.4, 12.3, 43.8)	(87.6 , 60.9 , 57.2)	(88.2 , 62.2 , 62.3)

Evaluation metrics. We employ the Area Under the Receiver Operating Characteristic (AUROC), maximum F1 score (F1-max), and Average Precision (AP) for image-level classification; and AUROC, AP, and Per-Region Overlap (PRO) for pixel-level segmentation.

Implementation details. We employ a pre-trained CLIP (ViT-L-14-336) as the backbone. Patch features are extracted from the 6th, 12th, 18th, and 24th layers. We maintain a zero-shot setting by training on VISA and evaluating on the remaining datasets, and training on MVTEC-AD when evaluating VISA. The sequence length m is set to 2, the number of experts N to 8, and the Top- k parameter k to 2. The model is trained for 20 epochs with batch size 32 using Adam (initial learning rate 2×10^{-4}) on a single NVIDIA A100 GPU.

3.2. Main Results

As shown in Table 1, we compare WMoE-CLIP with five state-of-the-art methods: WinCLIP [1], CLIP-AD [20], AnomalyCLIP [6], AdaCLIP [4], and AA-CLIP [2]. WMoE-CLIP consistently outperforms these baselines. Compared to AA-CLIP, it improves image-level AUROC by 1.9% and 2.7% on MVTEC-AD and VISA, respectively. Although AA-CLIP adopts a two-stage training strategy, it struggles to capture fine-grained image features. In contrast, our method leverages wavelet transformation to extract frequency information, enabling more discriminative representations. Furthermore, results on eight medical datasets demonstrate WMoE-CLIP’s strong generalization, achieving state-of-the-art performance on both image-level and pixel-level metrics.

Figure 2 presents anomaly localization results on industrial and medical datasets. WMoE-CLIP achieves precise localization, particularly in challenging medical scenarios, benefiting from global semantic feature sampling and wavelet-enhanced alignment, which facilitate cross-modal interaction.

Table 2. Ablation studies with image-level AUROC (I-AUC) and pixel-level AUROC (P-AUC) metrics.

CTDS	WCMA	SA-MoE	MVTec-AD		VisA	
			I-AUC	P-AUC	I-AUC	P-AUC
			88.6	90.8	84.8	94.3
✓			89.9	91.4	85.5	94.9
✓	✓		90.9	91.8	86.1	95.3
✓		✓	91.5	91.6	86.7	95.1
✓	✓	✓	92.4	92.1	87.3	95.6

3.3. Ablation Study

We conducted ablation studies on the MVTEC-AD and VISA datasets, as shown in Table 2. CTDS models the global distribution, improving image-level and pixel-level AUROC by 1.3% and 0.6% on MVTEC-AD. WCMA facilitates multi-modal interaction and yields improvements of 1.0% and 0.4% for image-level and pixel-level AUROC on MVTEC-AD. SA-MoE enhances the image-level performance by integrating contextual information, resulting in an improvement of 1.2% on VISA. Combining all modules achieves the highest performance, demonstrating the effectiveness of our design.

4. CONCLUSION

In this paper, we propose WMoE-CLIP, a novel CLIP-based wavelet-enhanced mixture-of-experts prompt learning model for ZSAD. To improve the adaptability of text embeddings, CTDS models global features via distribution sampling and integrates rich global information into the prompts. WCMA leverages wavelet decomposition to extract multi-frequency image features. Moreover, SA-MoE dynamically aggregates contextual information, enabling robust perception of global semantics. Extensive experiments on industrial and medical datasets demonstrate the superior performance of our method.

5. REFERENCES

- [1] Jongheon Jeong, Yang Zou, Taewan Kim, Dongqing Zhang, Avinash Ravichandran, and Onkar Dabeer, “Winclip: Zero-/few-shot anomaly classification and segmentation,” in *Proceedings of the IEEE/CVF Conference on Computer Vision and Pattern Recognition*, 2023, pp. 19606–19616.
- [2] Wenxin Ma, Xu Zhang, Qingsong Yao, Fenghe Tang, Chenxu Wu, Yingtai Li, Rui Yan, Zihang Jiang, and S Kevin Zhou, “Aa-clip: Enhancing zero-shot anomaly detection via anomaly-aware clip,” in *Proceedings of the Computer Vision and Pattern Recognition Conference*, 2025, pp. 4744–4754.
- [3] Debesh Jha, Pia H Smedsrud, Michael A Riegler, Pål Halvorsen, Thomas De Lange, Dag Johansen, and Håvard D Johansen, “Kvasir-seg: A segmented polyp dataset,” in *International conference on multimedia modeling*. Springer, 2019, pp. 451–462.
- [4] Yunkang Cao, Jiangning Zhang, Luca Frittoli, Yuqi Cheng, Weiming Shen, and Giacomo Boracchi, “Ada-clip: Adapting clip with hybrid learnable prompts for zero-shot anomaly detection,” in *European Conference on Computer Vision*. Springer, 2024, pp. 55–72.
- [5] Peng Chen, Chao Huang, Yunkang Cao, Chengliang Liu, Wenqiang Wang, Mingbo Yang, Li Shen, Wenqi Ren, and Xiaochun Cao, “Reason-iad: Knowledge-guided dynamic latent reasoning for explainable industrial anomaly detection,” *arXiv preprint arXiv:2602.09850*, 2026.
- [6] Qihang Zhou, Guansong Pang, Yu Tian, Shibo He, and Jiming Chen, “Anomalyclip: Object-agnostic prompt learning for zero-shot anomaly detection,” *arXiv preprint arXiv:2310.18961*, 2023.
- [7] Peng Chen, Fangjun Huang, and Chao Huang, “Dyc-clip: Dynamic context-aware multi-modal prompt learning for zero-shot anomaly detection,” *Pattern Recognition*, p. 113215, 2026.
- [8] Paul Bergmann, Michael Fauser, David Sattlegger, and Carsten Steger, “Mvtec ad—a comprehensive real-world dataset for unsupervised anomaly detection,” in *Proceedings of the IEEE/CVF conference on computer vision and pattern recognition*, 2019, pp. 9592–9600.
- [9] Yang Zou, Jongheon Jeong, Latha Pemula, Dongqing Zhang, and Onkar Dabeer, “Spot-the-difference self-supervised pre-training for anomaly detection and segmentation,” in *European conference on computer vision*. Springer, 2022, pp. 392–408.
- [10] Pankaj Mishra, Riccardo Verk, Daniele Fornasier, Claudio Piciarelli, and Gian Luca Foresti, “Vt-adl: A vision transformer network for image anomaly detection and localization,” in *2021 IEEE 30th International Symposium on Industrial Electronics*. IEEE, 2021, pp. 01–06.
- [11] Jakob Božič, Domen Tabernik, and Danijel Skočaj, “Mixed supervision for surface-defect detection: From weakly to fully supervised learning,” *Computers in Industry*, vol. 129, pp. 103459, 2021.
- [12] Matthias Wieler and Tobias Hahn, “Weakly supervised learning for industrial optical inspection,” in *DAGM symposium in*, 2007, vol. 6, p. 11.
- [13] Toshimichi Aota, Lloyd Teh Tzer Tong, and Takayuki Okatani, “Zero-shot versus many-shot: Unsupervised texture anomaly detection,” in *Proceedings of the IEEE/CVF Winter Conference on Applications of Computer Vision*, 2023, pp. 5564–5572.
- [14] Mohammadreza Salehi, Niousha Sadjadi, Soroosh Baselizadeh, Mohammad H Rohban, and Hamid R Rabiee, “Multiresolution knowledge distillation for anomaly detection,” in *Proceedings of the IEEE/CVF conference on computer vision and pattern recognition*, 2021, pp. 14902–14912.
- [15] Pranita Balaji Kanade and PP Gumaste, “Brain tumor detection using mri images,” *Brain*, vol. 3, no. 2, pp. 146–150, 2015.
- [16] David Gutman, Noel CF Codella, Emre Celebi, Brian Helba, Michael Marchetti, Nabin Mishra, and Allan Halpern, “Skin lesion analysis toward melanoma detection: A challenge at the international symposium on biomedical imaging (isbi) 2016, hosted by the international skin imaging collaboration (isic),” *arXiv preprint arXiv:1605.01397*, 2016.
- [17] Nima Tajbakhsh, Suryakanth R Gurudu, and Jianming Liang, “Automated polyp detection in colonoscopy videos using shape and context information,” *IEEE transactions on medical imaging*, vol. 35, no. 2, pp. 630–644, 2015.
- [18] Jorge Bernal, F Javier Sánchez, Gloria Fernández-Esparrach, Debora Gil, Cristina Rodríguez, and Fernando Vilariño, “Wm-dova maps for accurate polyp highlighting in colonoscopy: Validation vs. saliency maps from physicians,” *Computerized medical imaging and graphics*, vol. 43, pp. 99–111, 2015.
- [19] Steven A Hicks, Debesh Jha, Vajira Thambawita, Pål Halvorsen, Hugo L Hammer, and Michael A Riegler, “The endotect 2020 challenge: evaluation and comparison of classification, segmentation and inference time

for endoscopy,” in *Pattern Recognition. ICPR International Workshops and Challenges: Virtual Event, January 10-15, 2021, Proceedings, Part VIII*. Springer, 2021, pp. 263–274.

- [20] Xuhai Chen, Jiangning Zhang, Guanzhong Tian, Haoyang He, Wuhao Zhang, Yabiao Wang, Chengjie Wang, and Yong Liu, “Clip-ad: A language-guided staged dual-path model for zero-shot anomaly detection,” in *International Joint Conference on Artificial Intelligence*. Springer, 2024, pp. 17–33.